Wavelength dependence of cells of finite depth in directional solidification

N. Ramprasad, M. J. Bennett, and R. A. Brown
Department of Chemical Engineering and Materials Processing Center, Massachusetts Institute of Technology, Cambridge, Massachusetts 02139
(Received 21 September 1987)

Finite-element calculations are presented for the two-dimensional cellular interface shapes in a spatially periodic microstructure that occurs during the directional solidification of a dilute binary alloy. The transition from small-amplitude sinusoidal shapes to cells separated by deep grooves as the growth rate is increased is computed as a function of spatial wavelength. The flatness of the neutral stability curve of growth rate versus spatial wavelength is responsible for secondary bifurcations that lead to tip splitting of the cells and to an apparent decrease in the wavelength of the pattern. Deep cells with round tips, long linear grooves, and pendant-shaped bottoms are computed for continuous ranges of wavelength and growth rate. A wavelength corresponding to the cell with maximum aspect ratio is computed as a function of the growth rate.

I. INTRODUCTION

The analysis of the formation of cellular and dendritic patterns in solidification microstructures is receiving increasing attention. Some of this interest results from the importance of the microstructure in determining the electrical and mechanical properties of the solid. The formation of microstructure during solidification also is an example of pattern formation in a system controlled by bulk and interfacial transport mechanisms. Furthermore, because the length scale for the structure is small compared to the sample size, it is improbable that the boundaries of the system play any role in selection of the morphology. Several differing viewpoints have been taken in searches for mechanisms of spatial pattern selection in such systems. A critical issue is whether or not there is a single mechanism for selecting a particular spatial pattern or whether the resulting pattern is a result of nonlinear dynamic, and most likely chaotic, interactions of the pattern over a range of time and length scales. Both approaches seem to have credibility for specific mathematical models of solidification.

We consider these issues for the formation of cellular interfaces during the directional solidification of a thin, two-dimensional sample. Here a dilute binary alloy is solidified by moving the melt and solid trapped between two bounding surfaces through a unidirectional constant temperature gradient. For set alloy composition in the bulk melt and a specified temperature gradient, a planar interface morphology becomes unstable at a critical value of the growth rate to small-scale deformations of the interface which lead to cellular and dendritic patterns for larger growth rates. As V is increased the cells deepen and the wavelength of the pattern evolves, as has been observed in the many elucidating experiments based on thin-film solidification systems.[1-4]

The linear stability analysis of Mullins and Sekerka[5] first described the onset of these transitions as the appearance of a small amplitude sinusoidal deformation of the interface. This onset appears at a specific wavelength $\tilde{\lambda}(V_c)$ which corresponds to the lowest value of the growth rate $V=V_c$ for the instability. For $V>V_c$ the planar interface is linearly unstable to a range of wavelengths, as is shown in Fig. 1 for the set of physical properties used in the simulations described here. The nonlinear cell shapes that exist for $V>V_c$ select between these values in experiment.

The lower portion of the neutral stability curve shown in Fig. 1 is *qualitatively* similar to ones corresponding to other mathematical problems governing transitions in other transport systems, such as natural convection in layers heated from below and the onset of secondary vortices in Taylor-Couette flow. However, there is an important quantitative difference between the stability of these fluid mechanical systems and the solidification problem. The small-surface free energy that is typical for the melt/crystal interface in solidification systems is ineffective as a mechanism for stabilizing perturbations to the interface, except for spatial wavelengths that are much smaller than the critical value $\tilde{\lambda}_c$. This scaling causes the neutral stability curve predicted by linear theory to be extremely flat for wavelengths near $\tilde{\lambda}_c$. Qualitatively, the flatness results in a fairly large band of wavelengths becoming unstable at nearly the same value of growth rate. This result impacts the nonlinear interactions for finite amplitude cells, as is brought out below.

Several approaches to the analysis of wavelength selection have been applied to directional solidification models. These are loosely separated into three categories: (1) dynamic analysis of models for a nonlinear moving-boundary problem assuming specific sample sizes for the system; (2) asymptotic analysis that explicitly decouples long- and short-length scale interactions for a large collection of similar cells; and (3) selection mechanisms based on the existence of a singular limit which can only be reached for a particular value of the wavelength. A review of these perspectives is relevant to the discussion of the calculations presented here.

Bifurcation analysis has been used to compute families of weakly nonlinear cell shapes that evolve from the pla-

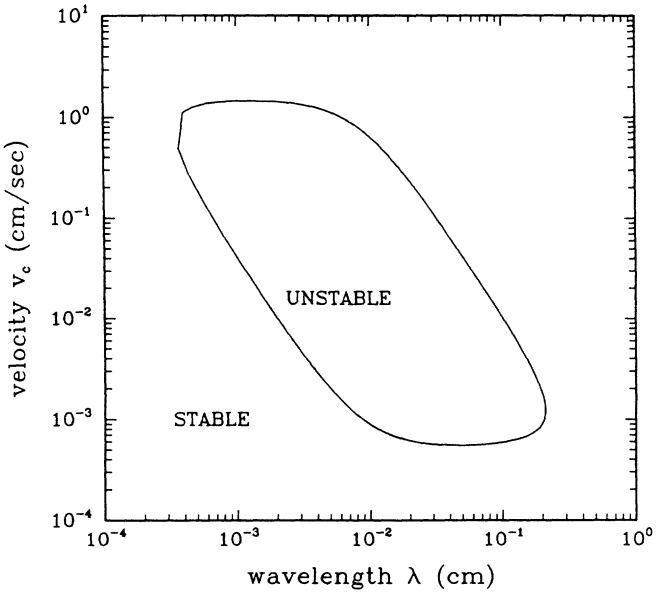

FIG. 1. Neutral stability diagram for two-dimensional directional solidification computed using thermophysical properties used in calculations reported here.

nar form for the range of spatial wavelengths allowed by linear theory.[6,7] Whether the bifurcation is initially subcritical or supercritical with respect to increasing V was shown by numerical calculations[7,8] to be unimportant in terms of the transitions to deep cells, because nonlinear folds in the solution families always seem to lead to finite-amplitude cellular forms for $V > V_c(\tilde{\lambda})$. A subcritical transition for $|V-V_c| \ll 1$ to $V < V_c$ only affects the experimental observability of the onset growth rate.[4,5]

Ungar and Brown[7] have shown that secondary bifurcations occur between families of cells with distinct and spatially resonant wavelengths. These bifurcations are the result of a codimension-two bifurcation point at $V=V^*$ which results when the wavelength $\tilde{\lambda}=\tilde{\lambda}^*$ is selected so that the linear theory predicts simultaneous bifurcation of shapes with the wavelengths $\tilde{\lambda}^*$ and $\tilde{\lambda}^*/2$. Haug[9] carried out the perturbation analysis about this codimension-two bifurcation and Bennett *et al.*[8] showed qualitative agreement between the structure of the solution families predicted by Haug and numerical calculations.

An important feature of the directional solidification system is that the flatness of the neutral stability curve causes these nonlinear transitions to appear within an extremely small range of growth rate, i.e.,

$$|V-V_c|/V_c < |V^*-V_c|/V_c \ll 1 . \quad (1.1)$$

Because of this feature, finite-amplitude cells with the most unstable wavelength predicted by linear theory only exist for a small range of V and are difficult to observe. We do not believe they have been successfully seen in any experiment.

The flatness of the neutral stability curve also places restrictions on the range of validity of asymptotic analysis for the evolution of long wavelength interactions between shallow cells.[10] Because the classical perturbation techniques pioneered by Newell and Whitehead[11] neglect interactions between spatially resonant modes on the length scale of the characteristic wavelength, results of these calculations are restricted to growth rates that satisfy (1.1). The calculations in Sec. III A demonstrate the secondary bifurcation between families of cells and set the range of validity of perturbation methods which neglect these nonlinear interactions.

Recently, much research has focused on the related problem of pattern selection in the solidification of needle-shaped crystals growing into a pure undercooled metal, the free-dendrite problem. Here the problem is to determine the relationship between the shape of the needle and the solidification rate. Langer[12] and others (see Refs. 13 and 14) have taken advantage of the exact family of parabolic crystal shapes that extend infinitely far back from the tip *without* surface free energy to construct asymptotic analyses which lead to a *solvability* condition for small-surface energies. In the asymptotic framework, this condition amounts to the requirement that the shape at the tip be symmetric so that no discontinuity is introduced. Meiron[15] and Kessler *et al.*[16] have shown that a boundary integral numerical calculation of the crystal shape will select the same value of the tip radius for a given velocity when the condition for a symmetric tip is used as a solvability condition.

Karma[17] carried over the numerical analysis of Meiron[14] to a model of cellular solidification by assuming that the shape of the groove separating adjacent cells is described by *the approximate relationship* first developed by Scheil[18] in which the groove is assumed to be slender and the effect of surface energy is neglected. In this approximation, the thickness of the melt layer between two cells goes smoothly to zero leaving a cusp between them at infinite depth. Boundary integral calculations using the symmetry of the cell at the tip as a solvability condition and the leading order approximation to the shape of cusplike sidewall as a far-field boundary condition predicted discrete values of the wavelength for existence of the steady-state cell shape as a function of the growth rate.

This prediction seems to be at odds with the numerical calculations presented by Ungar and Brown[19] for the solutal model of solidification with diffusion in the solid phase. Ungar and Brown used specialized finite-element methods to compute a continuous family of cell shapes with given spatial wavelength evolving from the planar form with increasing growth rate. The interface shapes for the deep cells had developed three distinct regions: a rounded tip connected to an almost linear sidewall that stretched down between adjacent cells to terminate at a smooth, small-pendant bottom. A schematic of this type of form is shown in Fig. 2. Although calculations in this paper focused on cells with wavelengths that were integer multiples of the critical value $\tilde{\lambda}_c$, there is evidence that these calculations could be repeated with other linearly unstable wavelengths in a way that would be self-consistent with the existence of smooth cellular interfaces described by bifurcation analysis near the onset of cellu-

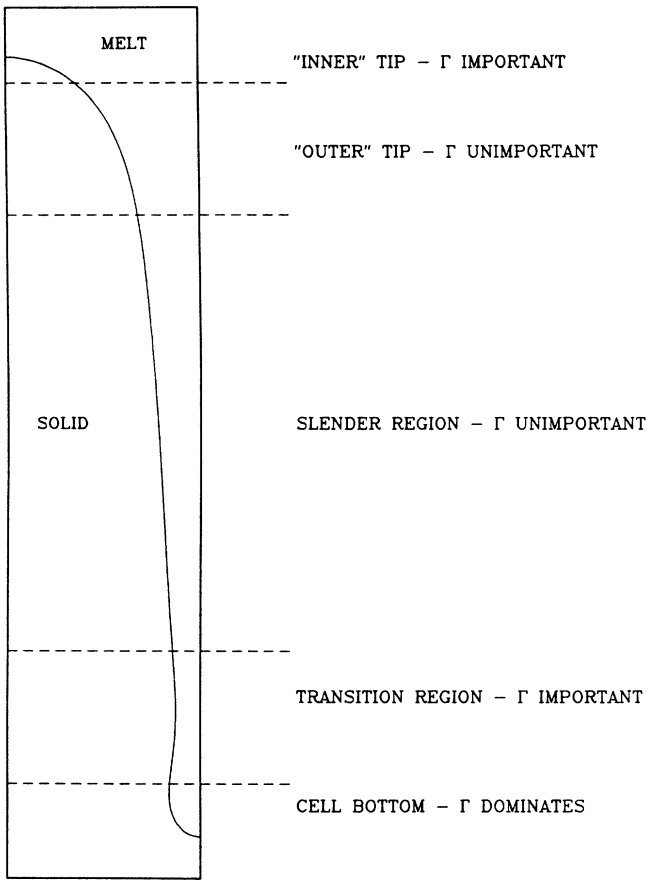

FIG. 2. Regions of deep cellular interface shape.

lar growth. Other numerical calculations[19,20] also have demonstrated the existence of steadily solidifying shallow cells for specific values of the wavelength.

The main purpose of this paper is to show that smooth, steadily-growing cellular interface shapes of finite depth are possible for a range of wavelengths. Therefore no mechanism for wavelength selection based solely on the existence of steady forms is possible when the cell has finite depth so that the interface joins smoothly between adjacent cells at the bottom of the groove which separates them. We show this by calculations using the finite-element analysis described elsewhere[21,22] to compute these forms as either the growth rate or wavelength is varied.

II. TWO-SIDED SOLUTAL MODEL AND NUMERICAL METHODS

A. Formulation

The two-sided solutal model of directional solidification is a reduced form of the more general model for microstructure formation.[23] The temperature field in both melt and solid is taken to be linear in the direction of crystal growth and constant in the direction perpendicular to growth. This profile is assumed to be unaffected by changes in the shape of the interface and is consistent with the thermal conductivities being equal in both phases and the release of latent heat at the interface being unimportant. Solute diffusion in both the melt and solid are included in the model.

The model is written in dimensionless form with the length scales for the coordinates scaled with a reference scale λ^o, time with the diffusion time scale λ^{o2}/D_m (D_m is the diffusion coefficient) in the melt, temperature with the melting temperature of the pure material at a planar interface T_m^o, and concentration with the composition of the melt far in front of the interface c_o. The dimensionless solute balances in melt and crystal are written in a frame of reference moving with the steady-state solidification rate V as

$$\nabla^2 c + P\frac{\partial c}{\partial y} = \frac{\partial c}{\partial t} \tag{2.1}$$

in the melt, and

$$R_m \nabla^2 c + P\frac{\partial c}{\partial y} = \frac{\partial c}{\partial t} \tag{2.2}$$

in the solid, where y is the coordinate in the direction of growth, $R_m \equiv D_s/D$ is the ratio of the mass diffusivities in the solid and melt, and $P \equiv \lambda^o V/D_m$ is the solutal Peclet number. The solute diffusivity in the solid phase is included so that the melting and resolidification that occurs with reentrant cell shapes can be handled in a self-consistent manner.

The concentrations in the two phases at the melt/solid interface are related through the phase diagram as

$$c_s = kc_m \ , \tag{2.3}$$

where k is the equilibrium segregation coefficient and the subscripts s and m denote terms that are evaluated at the interface from the solid and melt phases, respectively.

Solute conservation at the interface requires

$$(\mathbf{n}\cdot\nabla c)_m + R_m(\mathbf{n}\cdot\nabla c)_s = (\mathbf{n}\cdot\mathbf{e}_y)[P + V_e(t)](k-1)c_m \ , \tag{2.4}$$

where $V_e(t)$ is the dimensionless vertical component of the interfacial velocity *in excess* of P and $\mathbf{e}_y$ is the unit vector in the direction of growth.

The interface shape is determined from the Gibbs-Thomson condition for interfacial equilibrium

$$(T_{\text{ref}} - 1)/m + (G/m)y = c_m + 2H(\Gamma/m) \ , \tag{2.5}$$

where H is the dimensionless local mean curvature of the interface, m is the dimensionless slope of the liquidus curve (scaled with T_m^o/C_o), Γ is the dimensionless capillary length, and G is the dimensionless temperature gradient scaled with T_m^o/λ^o. Equation (2.5) expresses the dependence of the melting temperature on the composition of the melt at the interface ($m \cdot c$) and the surface energy and local curvature ($\Gamma \cdot 2H$). The constant T_{ref} is a reference temperature that is set so that the interface is positioned in the computational domain; the quantity $(T_{\text{ref}} - 1) = 40.2 \times 10^{-5}$ for the calculations reported here.

The small influence of the surface energy on selecting

the wavelengths for linear stability and the asymptotic analyses described in Sec. I are results of the appropriate scales for the dimensionless groups that appear in the Gibbs-Thomson equation. The values of the parameters used in the simulations described here are listed in Table I and are representative of a Pb-Sb alloy, but with the diffusivity ratio R_m set to one instead of the small values $(1\times10^{-2}-1\times10^{-4})$ that would be more appropriate. The reference length scale of $\lambda^o=100\ \mu$m is characteristic of the critical wavelength for the onset of the instability. The important feature of these parameters is that the length scale associated with the surface energy $O(\Gamma/m)$ is 2 orders of magnitude smaller than the scales that are appropriate for the temperature gradient $O(G/m)$ and the solute diffusion layer $O(P^{-1})$ ahead of the interface. Because the surface energy is the primary mechanism for selecting the lateral scale for the interface structure, the mechanism for determining this dimension can be expected to be weak.

The neutral stability curve $V_c(\lambda)$ predicted by linear stability analysis is shown as Fig. 1 for these parameters. The variables are given in dimensional form. The dimensional growth rate and wavelength that correspond to the first cellular form are $(\tilde{V}_c,\tilde{\lambda}_c)=5.55\ \mu$m/sec, 459 μm). The flatness of the curve near the critical value is most evident when it is compared with similar curves that describe wavelength selection *at onset* for other instabilities. For example, when the curve $\tilde{\lambda}/\tilde{\lambda}_c$ versus $[P_c(\lambda)-P_c(\lambda_c)]/P_c(\lambda_c)$ is compared with the neutral stability curve for the critical value of the Rayleigh number $\mathcal{R}(\lambda)$ as a function of wavelength for the analogous two-dimensional Rayleigh-Bénard instability between parallel, shear-free surfaces (plotted as $[\mathcal{R}_c(\lambda)-\mathcal{R}_c(\lambda_c)]/\mathcal{R}_c(\lambda_c)$] as a function of $\tilde{\lambda}/\tilde{\lambda}_c$) the neutral stability curve for the directional solidification problem is 2 orders of magnitude flatter near λ_c than the curve for the fluid mechanical system.

Another important difference between the solidification problem and the fluid systems is that the neutral stability curves for directional solidification are closed for constant temperature gradient G and composition c_o. The planar interface is restabilized at high growth rates by the shrinking of the diffusion boundary layer in which perturbations are stabilized by diffusion and surface energy.

TABLE I. Values of dimensionless parameters used in the solutal model.

Dimensionless group	Value
Segregation coefficient k	0.4
Diffusivity ratio $R_m\equiv D/D_s$	1.0
Dimensionless temperature gradient $G\equiv\tilde{G}\lambda^o/T$	4.5×10^{-5}
Dimensionless liquidus slope $m\equiv\tilde{m}c_o/T_m^o$	-1.67×10^{-4}
Dimensionless capillary length $\Gamma\equiv\tilde{\Gamma}T_m^o/\lambda^o$	8.2×10^{-7}
Reference length scale λ^o	100 μm

This upper bound for instability suggests that cellular and dendritic morphologies will not be observed for unbounded growth rates, although for the physical parameters analyzed here there is a 4 order-of-magnitude difference in the growth rates between the lower and upper stability curves. Mullins and Sekerka[1] coined the phrase "absolute stability limit" to describe the upper branch of the neutral stability curve.

B. Finite-element analysis

Full numerical solution of the free- and moving-boundary problems described by Eqs. (2.1)–(2.7) is an effective method for determining the structure of steadily solidifying and dynamically changing deep cellular interfaces. We have developed finite-element Newton methods[21,22] that compute the steadily solidifying cellular forms with given wavelength and lead to computer-implemented perturbation methods for determining the stability of these forms and the existence of bifurcations to other shape families. These methods are based on using nonorthogonal transformations to map the shape of the melt/solid interface and the regions of melt and solid to a fixed domain where the interface is a coordinate surface. The transformed field equations (1) and (2) are discretized by a two-dimensional Galerkin finite-element approximation which incorporates the solute balance at the interface (2.4) and the symmetry condition (2.5) as natural boundary conditions. The Gibbs-Thomson condition is written in weak form as a one-dimensional residual equation for the interface shape with the symmetry conditions on the shape of the interface (2.7) incorporated as natural boundary conditions. The resulting set of algebraic equations for the coefficients in the finite-element representations of the solute field and the interface shape are solved by Newton's method.

Two different nonorthogonal transformations were used in the calculations described here. For nearly planar interfaces, the Mongé transformation $y=h(x,t)$ was used as described in Ref. 24. Deep cells cannot be represented by this transformation, because the groove between adjacent cells may be reentrant. Ungar and Brown[21] developed a "deep cell mapping" composed of cylindrical polar and rectangular Cartesian pieces to account for this possibility. The details of the implementation of the finite-element Newton method for this transformation are described in Ref. 22.

The calculations reported here were performed with different meshes for the two interface representations. The results for the Mongé representation $[y=h(x,t)]$ had 16 elements along the interface and 20 elements perpendicular to it, per half a wavelength of a cell. Results with the mixed Cartesian/polar interface representation had 60 elements along the interface and 20 elements in the perpendicular direction, with the elements distributed to maximize the accuracy of the calculation in the tip and bottom regions. As is discussed more fully in Ref. 22, this mesh size was selected by refining the discretization until the aspect ratio of the deepest cells changed by less than one percent on doubling of the number of elements.

III. FINITE-ELEMENT RESULTS

A. Calculations with fixed wavelength

The transition from the planar interface to deep cells for a specific spatial wavelength is exemplified by calculations for the most dangerous dimensionless wavelength $\lambda=\lambda_c\simeq 4.59$ predicted by linear stability theory. Calculations using the Mongé representation of the interface were performed using a sample size of $\lambda_c/2\simeq 2.30$ so that cells with wavelength $\lambda_c/(n+1)$ $n=0,1,\ldots$, are admissible in the computational domain. In this domain, families of cellular shapes with wavelengths $(\lambda_c, \lambda_c/2, \lambda_c/4, \ldots)$ bifurcate from the planar interface at critical values $[P_c(\lambda_c), P_c(\lambda_c/2), P_c(\lambda_c/4), \ldots]$. These shapes are represented in Fig. 3 by the dimensionless amplitude of the cell depth defined as

$$\Delta=\tilde{\Delta}/\lambda^o , \tag{3.1}$$

where $\tilde{\Delta}$ is the dimensional value of the depth.

The three families of shapes that bifurcate from the planar state with dimensionless wavelengths λ_c, $\lambda_c/2$, and $\lambda_c/4$ were computed by tracking these solution curves from the critical points along the planar family. The solid curves in Fig. 3 were computed using the Mongé interface representation. Two secondary bifurcation points were located that connect two of the solution families. Each is expected because of a codimension-two bifurcation point that exists *at another wavelength* between the two interacting cell shapes. Cells with wavelength λ_c were computed only up to the secondary bifurcation point where the family joined one with shapes of wavelength $\lambda_c/2$. This shape family evolved with P through a turning point $P=P_1\simeq 2.12$ and is connected to the family of $\lambda_c/4$ shapes at a secondary bifurcation point. Calculations with the Mongé transformation were stopped near this point because of the possibility that the interface shape was becoming reentrant. Deep cellular shapes in the $(\lambda_c/4)$ family were computed with the mixed cylindrical-Cartesian representation and are shown in Fig. 3 by the dotted curve. The mismatch between the results for the Mongé and mixed cylindrical-Cartesian representations occurs because of differences in the two finite-element discretizations.

Sample interface shapes from each family are shown in Fig. 4. The shape in the (λ_c) family shows the development of an indentation in the tip at very low amplitude as the beginning of the mechanism for tip splitting and formation of cell shapes in the $(\lambda_c/2)$ family. A similar evolution of the tip shape occurs in the shapes of the $(\lambda_c/2)$ family. The shapes in the $(\lambda_c/4)$ family become reentrant for the range of P shown in Fig. 3. For $P>2$, the cells have rounded tips, approximately linear sidewalls, and rounded bottoms. The bottom and the sidewall are connected through a transition regime where the interface becomes reentrant so that solid melts into the bottom.

An important feature of this diagram is the rapid change in the apparent spatial wavelength of the cells with increasing growth rate. Cells with wavelength near the critical value are only possible for a narrow range of

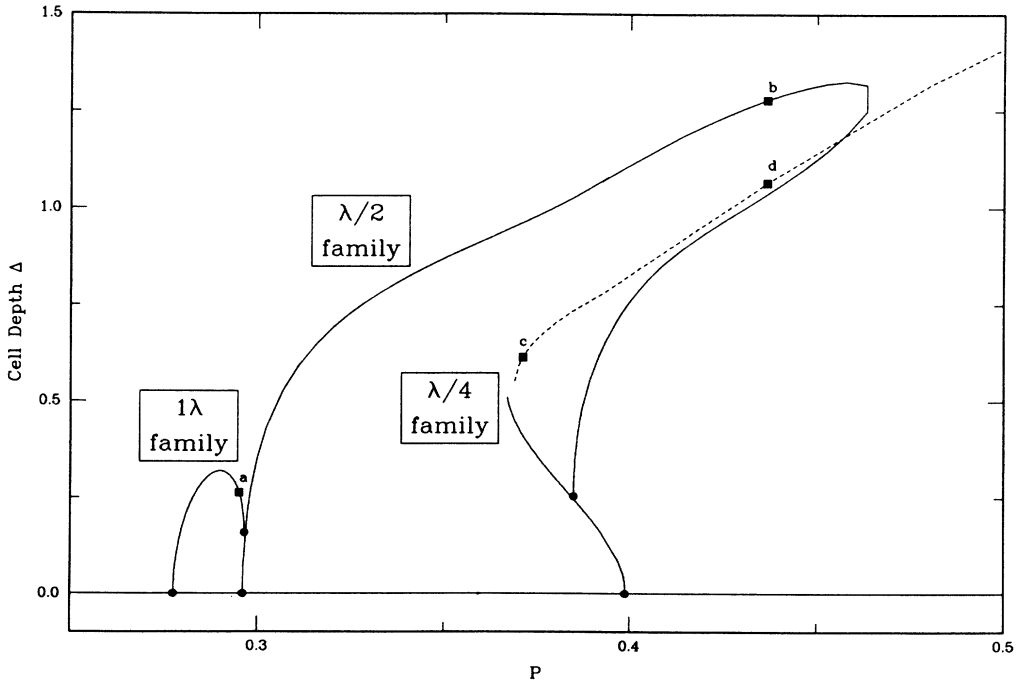

FIG. 3. Families of steady-state cellular shapes with spatial wavelengths that are an integer fraction of λ_c as computed by the two finite-element methods. The amplitude of the cell Δ is defined by Eq. (3.1). Solid curves correspond to shapes computed with the Mongé representation; the dashed portion of the $(\lambda_c/4)$ family was computed using the mixed cylindrical-Cartesian representation. Letters and points (■) correspond to positions for sample interface shapes shown in Fig. 4. Bifurcation points are denoted by (●).

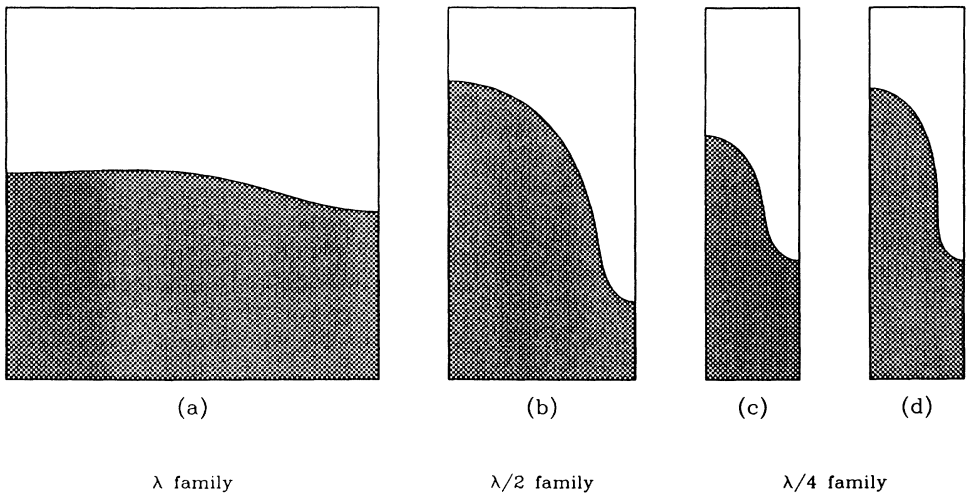

FIG. 4. Sample interfaces in each of the three shape families shown in Fig. 3. Letters correspond to points shown in that figure.

P and the wavelength splits to $\lambda_c/4$ *within less than a 50%* increase in P. The proximity of the value of P for these secondary transitions compared to the value of P for the onset of cellular solidification is a consequence of the flatness of the neutral stability curve $P=P_c(\lambda)$. Calculations with the same parameter values, but $R_m=0$ show that these transitions occur in even a smaller range of growth rate.[7]

The calculations shown in Fig. 3 for $\lambda=\lambda_c$ can be repeated for a range of wavelengths with only small changes in the connectivity of the bifurcation diagram. The bifurcation diagram computed for $\lambda=1$ using both interface representations is shown in Fig. 5. The family of cell shapes that evolves with the fundamental wavelength forms deep cells before any secondary bifurcation is detected. Cells with dimensionless wavelength $\lambda=1$

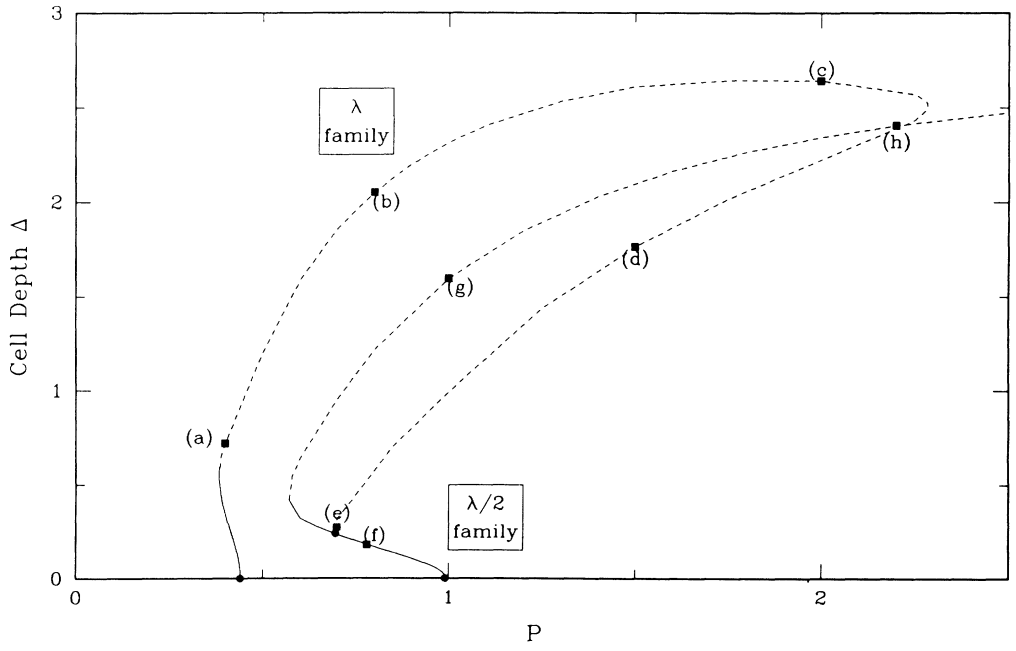

FIG. 5. Families of steady-state cellular shapes with spatial wavelengths that are an integer fraction of $\lambda=1$ as computed by the two finite-element methods. The amplitude of the cell Δ is defined by Eq. (3.1). Solid curves correspond to shapes computed with the Mongé representation and the dashed curve signifies calculations with the mixed cylindrical-Cartesian representation. Letters and points (■) correspond to positions for sample interface shapes shown in Fig. 6. Bifurcation points are denoted by (●).

exist only up to the turning point shown in this figure. The shapes in the reverse portion of this family evolve to lower values of P until a secondary bifurcation occurs which splits the wavelength to $\lambda=\frac{1}{2}$. Sample shapes in the $\lambda=1$ family are shown in Fig. 6. The deep cell representation can only be used to compute cell shapes for which the tip shape is single valued in the cylindrical polar representation used for that region, so the entire process of wavelength splitting cannot be calculated. The cells shown in Fig. 6 calculated along the reverse portion of the family with $\lambda=1$ develop flat tips and become slightly indented as P is decreased. These cells are still long and have narrow grooves and reentrant bottoms; however, the details of the bottom are changing with P. The sample shapes with wavelength $\lambda=\frac{1}{2}$ are similar to those for the larger wavelength, except that the bottom is enlarged because of the larger importance of surface energy. No limit point was detected in this family for the range of growth rates computed.

The deep cell shapes in Figs. 4 and 6 appear to have a particular asymptotic structure. The slope of the sidewall of the groove is approximately independent of P and only the absolute position of the cell and the length of the sidewall before the transition to the rounded bottom are changing with growth rate. The shape of the groove is well approximated by neglecting the influence of the surface free energy in the Gibbs-Thomson equation and noting that $(G/m)\sim 10^{-2}$ is a small parameter for these calculations. It is straightforward to show that the concentration field and interface are approximately

$$c(x,y)\simeq c_1+c_2(G/m)y+O((G/m)^2)\ , \tag{3.2a}$$

$$h(x,y)\simeq h_0+h_1(G/m)y+O((G/m)^2)\ , \tag{3.2b}$$

where h_0, h_1, c_1, and c_2 are constants that are determined by matching these results to solutions for the cell tip and bottom.

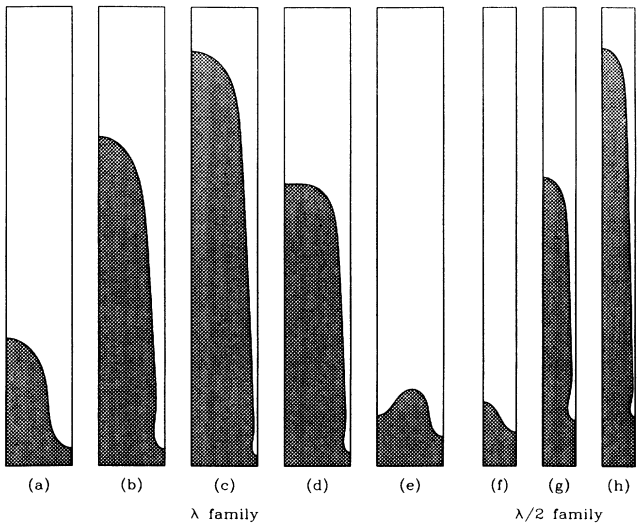

FIG. 6. Sample interfaces in each of the two shape families shown in Fig. 5. Letters correspond to points shown in that figure.

The slope of the concentration fields in melt and solid and of the interfaces predicted by Eqs. (3.2) closely match those in the calculations. The shape of this region is *independent* of the growth rate for the range of growth rate before the limit point. Equations (3.2) are the asymptotic limit for $(G/m)\ll 1$ of the expression for the shape of the groove developed by Scheil[18] and used by Karma[17] in numerical calculations of cells with infinite length.

B. Wavelength dependence of steady-state cell shape

Calculations were performed with specific values of the dimensional growth rate V, measured in units of the critical value $V_c=V(\tilde{\lambda}_c)$ and with varying dimensional wavelength $\tilde{\lambda}$. For decreasing wavelength and constant growth rate, the dimensionless values of the temperature gradient (G/m) and growth rate (P) decrease proportionally to $\tilde{\lambda}$ and the capillary length (Γ/m) increases as the inverse of $\tilde{\lambda}$, respectively.

Continuous families of cell shapes were computed for ranges of growth rate and wavelength. These families of cells are plotted in Fig. 7 as a function of the cell depth Δ for varying dimensionless wavelength and dimensional growth rate. For any growth rate, there is a deepest cell computed by the finite-element algorithm. The wavelength of this form decreases from the value λ_c for $V=V_c$ at the onset of solidification to values corresponding to the left side of the neutral stability curve.

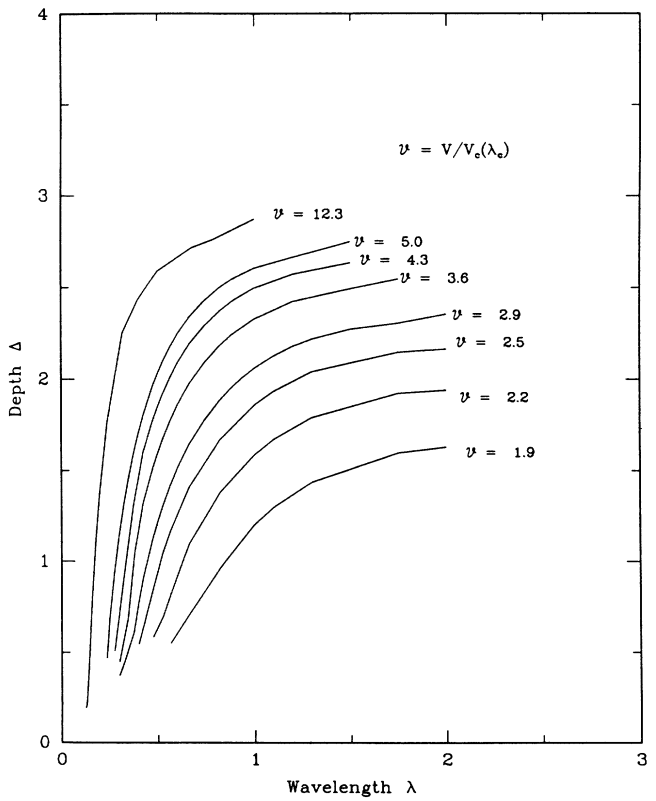

FIG. 7. Dependence of cell depth on spatial wavelength for specific values of the dimensionless growth rate $\mathcal{V}$.

With increasing V, finite amplitude cells are only seen for wavelengths below a decreasing maximum value. For the calculations examined here, the termination of the curves at the largest wavelength corresponds to the limit points observed for increasing P and constant λ. Near this limit the cellular form is nonunique; shorter cells exist on the branch with decreasing λ.

The maximum in the cell depth is more dramatically illustrated by replotting the curves on Fig. 7 as a function of the aspect ratio (Fig. 8) of the cell for each calculation as defined as

$$A \equiv \tilde{\Delta}/\tilde{\lambda} , \tag{3.3}$$

where $\tilde{\lambda}$ is the wavelength of the cell in the particular calculation. The peak of the curves $A = A(\lambda; v)$ sharpens with increased V and shifts toward the left boundary of the neutral stability curve.

The existence of a true asymptotic limit in which P and Δ tend to infinity as λ tends to a limiting value is impossible because of the closed shape of the neutral stability curves. Bennett *et al.*[8] have shown that the restabilization of the planar form for high Peclet numbers leads to shape families for finite amplitude cells for given λ that bifurcate from the planar form at the lower critical value of P and *reconnect* at the upper one. Then cells with smooth bottoms will not tend to infinite depth, no matter what wavelength is considered.

Sample cell shapes computed along the curve for $V = 2.9V_c$ are shown in Fig. 9. Cell shapes with the small wavelengths have bulbous bottoms caused by the increasing value of Γ. This bottom is connected to the cell tip through a thin groove. The depth of the cell decreases with decreasing λ as the thickness and the length of the groove is adjusted to accommodate the matching of the tip and enlarging bottom of the cell. Cell shapes computed for the largest wavelengths have small bottoms connected to a thin groove so as to accommodate the small value of Γ. The decreasing length of the cell results from the increasing value of the temperature gradient (G/m) with increasing λ which shortens the length of the sidewall needed to decrease the thickness of the liquid groove. The shape of the cell tip changes little with the varying wavelength. The maximum wavelength for calculations with a specific growth rate is caused by the envelope of turning points $P_1 = P_1(\lambda)$ in the families of deep cells illustrated in Figs. 3 and 5. When plotted on Fig. 7, the results illustrated in Figs. 3 and 5 correspond to vertical slices at the specific wavelengths.

Sample cell shapes in the family for $V = 12.3V_c$ are shown in Fig. 10 as examples of the deepest cells computed in this study. The structure of the cells described above also holds for this growth rate. The greater length of the cells at higher growth rate is a result of changes in the structure of the cell bottom, as noted in the calculations shown in Fig. 6 for changing P with fixed λ.

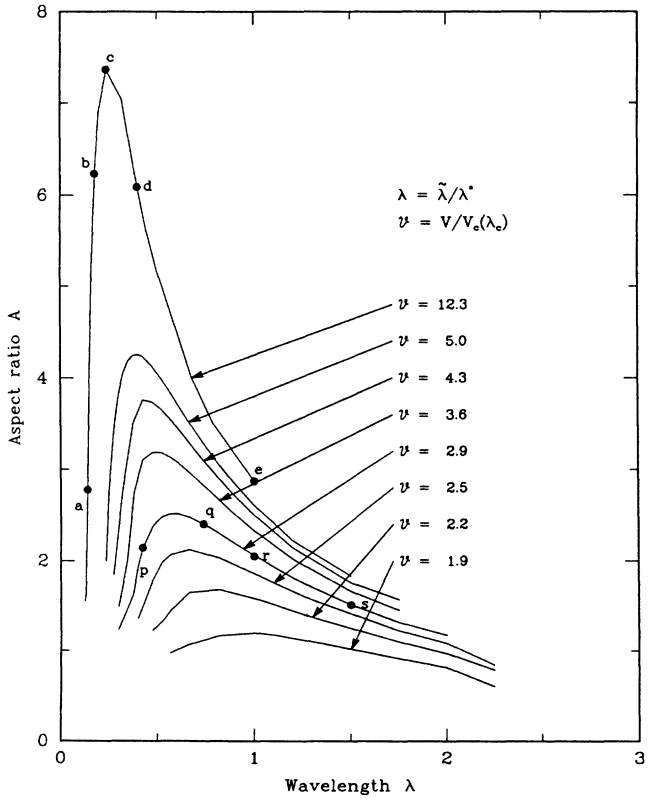

FIG. 8. Dependence of cell aspect ratio on spatial wavelength for specific values of the dimensionless growth rate $\mathcal{V}$.

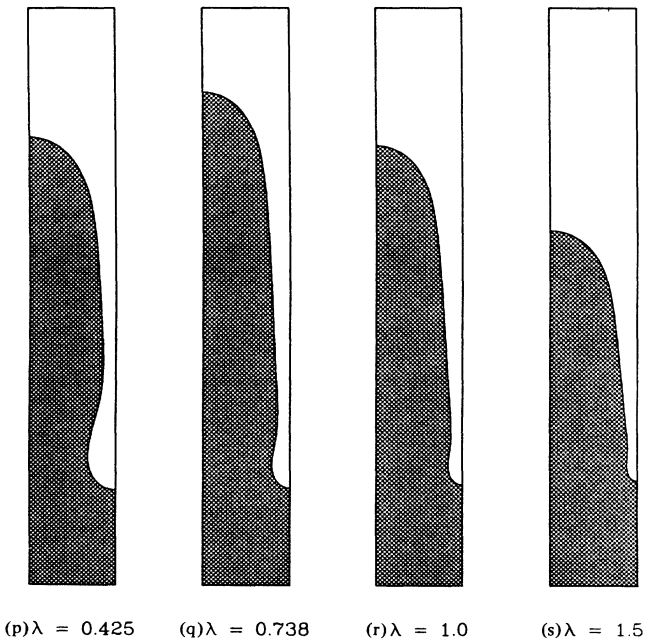

FIG. 9. Cell shapes for representative calculations from Fig. 8 and the growth rate, $\mathcal{V} = 2.9$. The letters correspond to the points shown there. The wavelengths have been normalized so that the aspect ratio of the cells, as measured by Δ, can be compared directly.

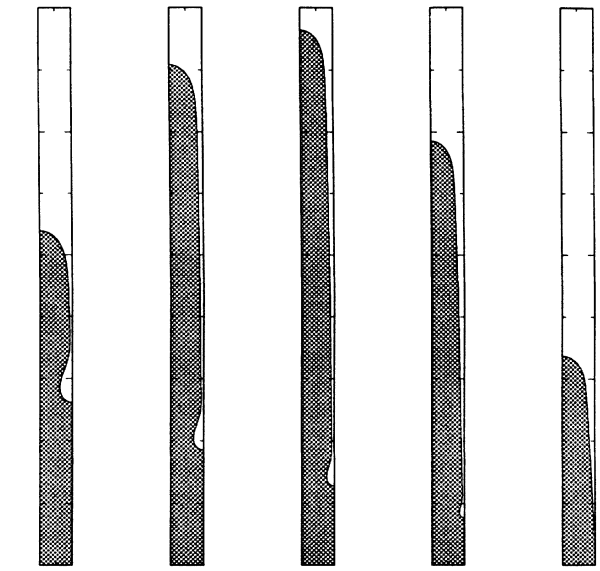

FIG. 10. Cell shapes for representative calculation from Fig. 8 and the highest growth rate $\mathcal{V}=12.3$. The letters correspond to the points shown there. The wavelengths have been normalized so that the aspect ratio of the cells, as measured by Δ, can be compared directly.

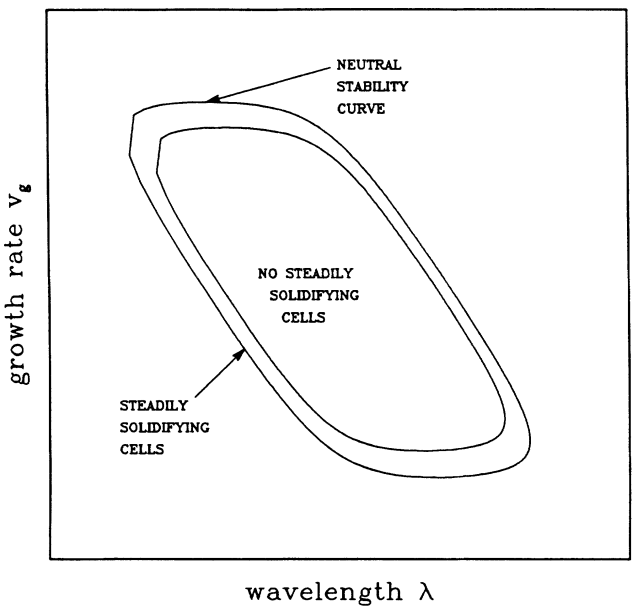

FIG. 11. Region for existence of steadily solidifying cells suggested by calculations and bifurcation analysis.

IV. DISCUSSION

Our calculations systematically bridge the gap between asymptotic predictions for small amplitude cells near the onset of cellular growth and the deep cells separated by narrow grooves that are seen in experiments. Two points are worthy of reemphasis. First, the small value of the surface energy appropriate for a melt/solid system leads to complex nonlinear transitions near the onset of the cells and to decreases in the apparent spatial wavelength caused by secondary bifurcation for small increases in the growth rate. Tip splitting by secondary bifurcation is not limited to shallow cells. It is observed for deep cells with reentrant bottoms; however, the family of shapes passes though a limit point and evolves to lower values of growth rate before the splitting takes place.

Most importantly, the calculations show that spatially-periodic, steadily-growing, two-dimensional cells with smooth shapes exist for ranges of the growth rate *and* wavelength, so that no mechanism for selection of a particular wavelength is found. The difference between these results and the analysis of Karma[16] is the smooth cell bottom predicted here for cells with finite depth. The surface energy Γ is paramount in setting the shape of the bottom and the transition zone between it and the linear sidewall. Indeed, the small-length scale of the bottom makes the curvature correction the dominant term in the Gibbs-Thomson equation (2.5). An asymptotic theory that describes the connection of the sidewall to the bottom will be presented elsewhere.

The calculations reported here suggest the picture shown in Fig. 11 for the existence of steady-state cellular shapes. Along the neutral stability curve there is a region of growth rates and spatial wavelengths in which at least one steadily solidifying cell exists. An enclosed region of wavelengths and growth rates is excluded. Tip splitting of shapes at constant wavelength and increasing growth rate leads to loss of existence of shapes with these wavelengths. A portion of the curve separating the regions has been identified by the calculations presented here to be associated with limit points in the family of solutions for the specific wavelength. The form of the bifurcation diagrams may evolve with changing wavelength so that the secondary bifurcation from the shapes with a given wavelength $\tilde{\lambda}$ and its harmonic $\tilde{\lambda}/2$ sets the bound on the existence of shapes. We have not attempted to compute the complete curve because of the amount of calculation that would be involved.

The connection between the continuous families of shapes predicted here and the discrete solutions predicted by Karma is an unanswered question. The answer must involve understanding of the stability of the shapes with smooth bottoms. Most probably, the cells with finite depth are unstable to a mechanism that leads to the pinching off of droplets of melt, as was first reported experimentally in Ref. 2. The spatial wavelength of a collection of cells undergoing such dynamics is most probably a statistical property.

ACKNOWLEDGMENTS

This research was supported by the Microgravity Sciences Program of the U. S. National Aeronautics and Space Administration. One of us (R. A. B.) was supported in part by the Camille and Henry Dreyfus Foundation. The authors are grateful to L. H. Ungar for many helpful discussions.

[1]K. A. Jackson and J. D. Hunt, Acta Metall. **13**, 1212 (1964).
[2]D. Venugopalan and J. S. Kirkaldy, Acta Metall. **32**, 893 (1984).
[3]S. De Cheveigné, C. Guthmann, and M. M. Lebrun, J Phys. (Paris) **47**, 2095 (1986).
[4]M. A. Eshelman and R. Trivedi, Acta Metall. **35**, 2443 (1987).
[5]W. W. Mullins and R. F. Sekerka, J. Appl. Phys. **34**, 444 (1964).
[6]D. J. Wollkind and L. A. Segel, Philos. Trans. R. Soc. London **268A**, 351 (1970).
[7]L. H. Ungar and R. A. Brown, Phys. Rev. B **29**, 1367 (1984).
[8]M. J. Bennett, R. A. Brown, and L. H. Ungar, in *The Physics of Structure Formation: Theory and Simulation,* edited by W. Guttinger and G. Dangelmyer (Springer-Verlag, New York, 1987).
[9]P. Haug, Phys. Rev. A **35**, 2733 (1987).
[10]G. Dee and R. Mathur, Phys. Rev. B **27**, 7073 (1984).
[11]A. C. Newell and J. A. Whitehead, J. Fluid Mech. **38**, 279 (1969).
[12]J. S. Langer, Phys. Rev. A **33**, 435 (1986).
[13]B. Caroli, C. Caroli, and B. Roulet, Phys. Rev. A **33**, 442 (1986).
[14]J. S. Langer and D. C. Hong, Phys. Rev. A **34**, 1462 (1986).
[15]D. I. Meiron, Phys. Rev. A **33**, 2704 (1986).
[16]D. A. Kessler, J. Koplik, and H. Levine, Phys. Rev. A **33**, 2253 (1986).
[17]A. Karma, Phys. Rev. A **34**, 4353 (1986).
[18]E. Scheil, Z. Metallkd. **34**, 70 (1942).
[19]G. B. McFadden and S. R. Coriell, Physica D **12**, 253 (1987).
[20]A. A. Wheeler, Q. J. Appl. Mech. **39**, 381 (1987).
[21]L. H. Ungar and R. A. Brown, Phys. Rev. B **31**, 5931 (1985).
[22]L. H. Ungar, N. Ramprasad, and R. A. Brown, J. Sci. Comput. (to be published).
[23]L. H. Ungar, M. J. Bennett, and R. A. Brown, Phys. Rev. B **31**, 5923 (1985).
[24]H. M. Ettouney and R. A. Brown, J. Comput. Phys. **49**, 118 (1983).

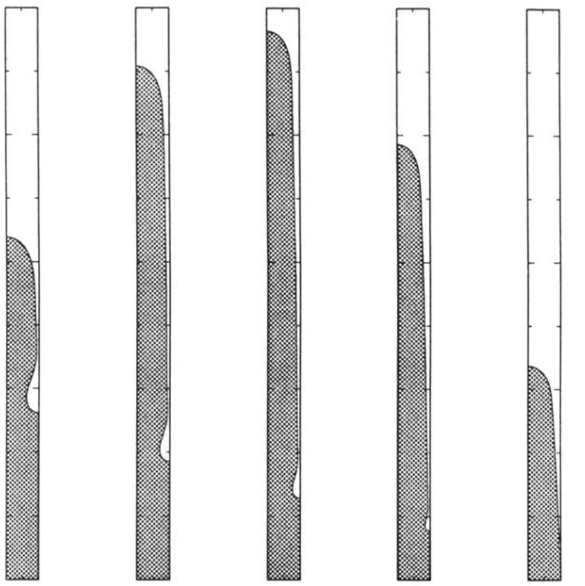

(a) $\lambda = 0.14$ (b) $\lambda = 0.18$ (c) $\lambda = 0.24$ (d) $\lambda = 0.40$ (e) $\lambda = 1.0$

FIG. 10. Cell shapes for representative calculation from Fig. 8 and the highest growth rate $\mathcal{V} = 12.3$. The letters correspond to the points shown there. The wavelengths have been normalized so that the aspect ratio of the cells, as measured by Δ, can be compared directly.

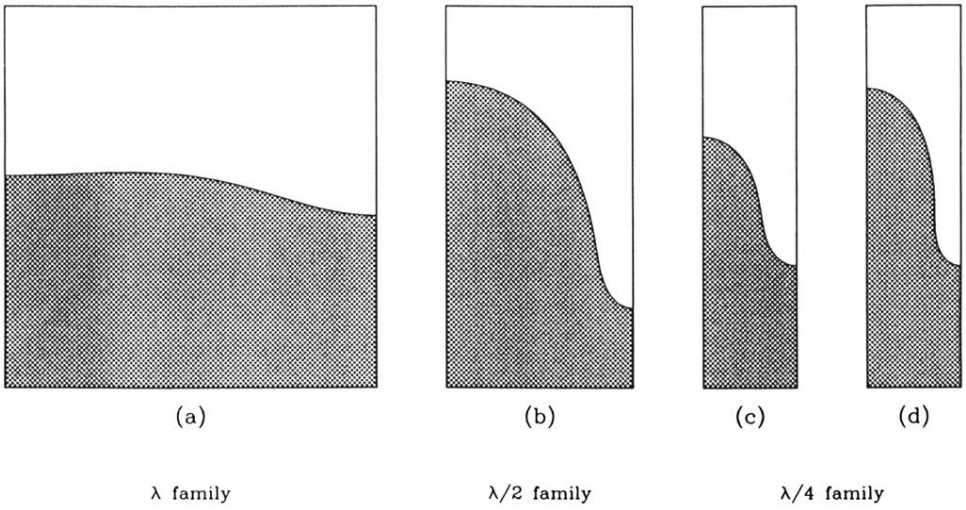

FIG. 4. Sample interfaces in each of the three shape families shown in Fig. 3. Letters correspond to points shown in that figure.

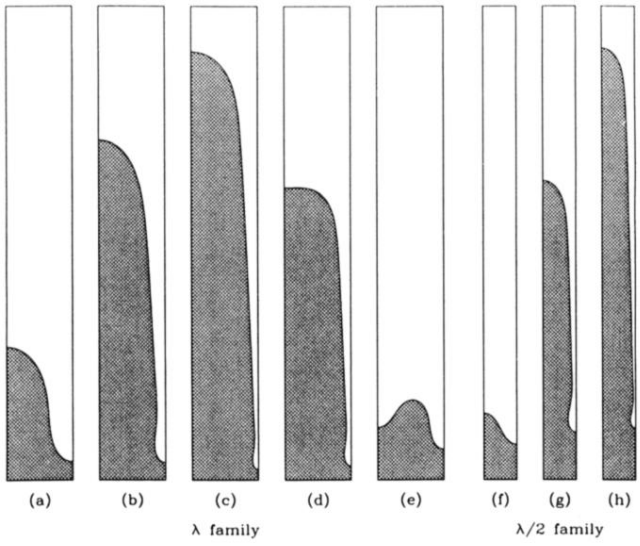

FIG. 6. Sample interfaces in each of the two shape families shown in Fig. 5. Letters correspond to points shown in that figure.

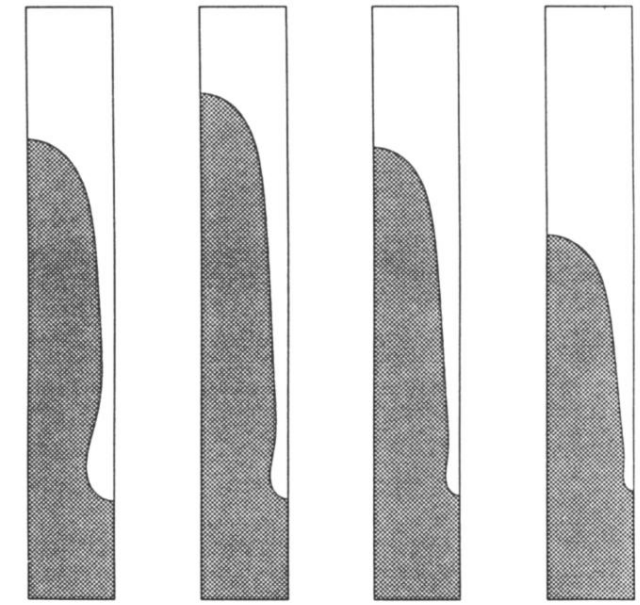

FIG. 9. Cell shapes for representative calculations from Fig. 8 and the growth rate, $\mathcal{V}=2.9$. The letters correspond to the points shown there. The wavelengths have been normalized so that the aspect ratio of the cells, as measured by Δ, can be compared directly.